Earth and Space Science

Correspondence to:
W. Chen,
wjchen@njtech.edu.cn

Moho Depth Estimation Beneath Tibet From Satellite Gravity Data Based on a Condensation Approach

Wenjin Chen[1] , **Robert Tenzer[2]**, **Xinyu Xu[3]** , **Shuai Wang[1]** , and **Bin Wang[1]**

[1]School of Geomatics Science and Technology, Nanjing Tech University, Nanjing, China, [2]Department of Land Surveying and Geo-Informatics, Hong Kong Polytechnic University, Hong Kong, [3]School of Geodesy and Geomatics, Wuhan University, Wuhan, China

Abstract We develop an algorithm for a Moho depth recovery from gravity and gravity gradiometry data and apply this method to estimate the Moho depth beneath the Tibetan Plateau. The basic idea of this algorithm is to describe mathematically the Moho depth undulations in terms of a condensation layer with respect to a mean Moho depth, instead of applying more commonly used isostatic compensation schemes. Expressions that functionally relate gravity field quantities with a (Moho) condensation layer are derived in spectral and spatial domains. The main advantage of this algorithm is that a functional relation between gravity field quantities and surface density anomalies, and consequently Moho depth undulations, has a linear form. The proposed algorithm is tested using satellite gravity and gravity gradiometry data. The Moho depth (taken with respect to the geoid surface) estimates obtained based on applying this algorithm are validated against global and regional seismic Moho results at the study area of Tibet. We also compare the result with the corresponding Moho depth estimates obtained by applying the Parker–Oldenburg and Vening Meinesz–Moritz (VMM) methods. The validation shows that results from all three gravimetric methods are similar, and they also closely agree with a regional seismic Moho model. Nevertheless, the VMM method and our algorithm in this comparison overperform the Parker–Oldenburg's method. The analysis of results also reveals that the newly developed algorithm provides better result (in terms of the RMS fit with a regional seismic Moho model) when applied for a Moho determination from gravity gradiometry instead of gravity data.

1. Introduction

A Moho recovery is one of a classical geophysical inversion problem, which is typically realized using results from seismic tomographic surveys (e.g., Bassin et al., 2000; Laske et al., 2013; Lebedev et al., 2013; Meier et al., 2007; Mooney et al., 1998; Nataf & Ricard, 1996; Shapiro & Ritzwoller, 2002; Soller et al., 1982). Since seismic data over large parts of the world are still not yet available or their coverage is limited and irregular, products from the Earth's satellite observation systems are used in gravimetric or gravimetric–seismic methods for a Moho recovery. This became particularly relevant after launching two gravity-dedicated satellite missions, the Gravity Recovery and Climate Experiment (GRACE) (Tapley, Bettadpur, Ries, et al., 2004; Tapley, Bettadpur, Watkins, et al., 2004) and the Gravity field and steady-state Ocean Circulation Explorer (GOCE) (e.g., Floberghagen et al., 2011) that provide information about the Earth's gravity field globally with high accuracy and relatively high resolution (∼80 km on equator). Gravimetric methods for a Moho recovery require topographic information that is globally provided from satellite altimetry missions, such the Shuttle Radar Topography Mission. Bathymetric information offshore is obtained from processing Sea Surface Topography (SST) data from the TOPEX/Poseidon, Jason-2, and other satellite altimetry missions by means of converting relative SST changes into corresponding relative marine gravity changes that are then used to predict the seafloor relief.

Various algorithms have been developed for a gravimetric Moho recovery. The Parker–Oldenburg's method (Oldenburg, 1974; Parker, 1972) is probably the most widely used for this purpose. Parker (1972) derived a gravity forward modeling formula to calculate gravity caused by an uneven, uniform material layer by means of a Fourier series. Later, Oldenburg (1974) rearranged the forward modeling formula in order to find the depth of density interface iteratively from gravity profiles. Braitenberg et al. (1997) developed independently an iterative scheme in which the inversion is carried out in the spectral domain, and the forward calculation with prisms is done in the spatial domain. Braitenberg et al. (2000) applied this method to determine the

Moho geometry in Tibet. Gómez-Ortiz and Agarwal (2005) generalized the Parker–Oldenburg's method for a 3D gravity inversion. The Parker–Oldenburg's method been applied in local and (small-scale) regional studies, for instance, by Rui (1985), Reamer and Ferguson (1989), Ferguson et al. (1988), Tiberi et al. (2001), Tirel et al. (2004), Gómez-Ortiz and Agarwal (2005), Shin et al. (2006, 2007, 2015), Chappell and Kusznir (2008), Kiamehr and Gómez-Ortiz (2009), Block et al. (2009), Prutkin and Saleh (2009), Hsieh et al. (2010), Steffen et al. (2011), Gómez-Ortiz et al. (2011), Bagherbandi (2012), Jiang et al. (2012), Aitken et al. (2013), Prasanna et al. (2013), Van der Meijde et al. (2013, 2015), Zhang et al. (2015), and Grigoriadis et al. (2016). The application of this method in (large-scale) regional, continental, or global studies is, however, somehow restricted by the fact that this method is formulated in the frame of the Cartesian planar topocentric coordinates, while disregarding the Earth's sphericity.

For global and large-scale regional studies, the Vening Meinesz–Moritz (VMM) method (Moritz, 1990; Sjöberg, 2009; Vening Meinesz, 1931) is preferably used. Mathematical foundations of this method were formulated by Moritz (1990). He extended the Vening Meinesz's isostatic hypothesis from regional to global model and derived an iterative algorithm for a Moho recovery from isostatic gravity anomalies. Later, Sjöberg (2009) reformulated Moritz's problem by means of solving the (nonlinear) Fredholm's integral equation of the first kind and called it the VMM's inverse problem of isostasy. The VMM functional model comprises linear spectral terms as well as the (second-order) spatial term that is solved by means of surface integrals. Consequently, the solution of VMM inverse problem is numerically relatively complex and time consuming because it involves a global integration to solve the second-order term. The Parker–Oldenburg's method is, on the other hand, numerically more efficient but applicable only for local and (small-scale) regional studies due to disregarding the Earth's sphericity.

In this study, we developed an alternative algorithm for a regional/global gravimetric Moho recovery in spatial and spectral domains that are functionally simple and numerically very efficient. This is possible because gravity changes are proportionally related to density changes. To facilitate this linear functional model between gravity and density changes in the context of a gravimetric Moho recovery, we first defined the Moho depth undulations in terms of a condensation layer with respect to a mean Moho depth. We then used a linear relationship between gravity and surface density to derive the expressions for a Moho recovery from gravity data and provided also respective expressions for gravity gradiometry data. Our functional model assumes a variable density contrast at the Moho interface and takes into consideration the Earth's sphericity but. Moreover, as mentioned above, this method is also numerically more efficient than the VMM or Parker–Oldenburg's methods.

The study is organized into four sections. Functional models are derived in Section 2. These functional models are then tested using real data to estimate the Moho depth beneath Tibet in Section 3. Results are presented in Section 4 and discussed in Section 5. The study is concluded in Section 6. We note that in this study we mainly focus on a validation of newly developed algorithms rather than tectonic and geological interpretation of results.

2. Functional Models

In this section, we derived functional models for a gravimetric Moho recovery from gravity and gravity gradiometry data in terms of a condensation layer in spherical and spatial domains.

2.1. Functional Models in Spectral Domain

We first define the Moho depth undulations in terms of a single condensation layer on a sphere of which radius is defined as $R' = R - D_0$, where R is the Earth's mean radius and D_0 denotes the mean Moho depth. The gravitational potential δT generated by the Moho depth undulations can then be described by the following surface integral:

$$\delta T\left(r,\theta,\lambda\right) = G \iint_{\Sigma} \frac{\kappa\left(\theta',\lambda'\right)}{l\left(r,\theta,\lambda,R',\theta',\lambda'\right)} d\Sigma,$$

(1)

where $l\left(r,\theta,\lambda,R',\theta',\lambda'\right)$ is the Euclidian's spatial distance between a computation point $\left(r,\theta,\lambda\right)$ and an integration point $\left(R',\theta',\lambda'\right)$, $d\Sigma = \left(R - D_0\right)^2 d\sigma$ is an infinitesimal surface element ($d\sigma$ denotes a unit sphere), and Σ is the total integral surface.

We further define the surface density anomaly $\kappa\left(\theta,\lambda\right)$ as a function of the (variable) Moho density contrast $\Delta\rho$ and the Moho undulation h (with respect to D_0). We write

$$\kappa\left(\theta,\lambda\right) = \Delta\rho\left(\theta,\lambda\right)h\left(\theta,\lambda\right). \tag{2}$$

To find a functional model for a gravimetric Moho recovery in spectral domain, we first define the reciprocal spatial distance l^{-1} in Equation 1 as follows (e.g., Heiskanen & Moritz, 1967):

$$\frac{1}{l\left(r,\theta,\lambda,R',\theta',\lambda'\right)} = \sum_{n=0}^{\infty} \frac{\left(R - D_0\right)^n}{r^{n+1}} P_n\left(\cos\psi\right), \tag{3}$$

where $\cos\psi$ reads

$$\cos\psi = \cos\theta\cos\theta' + \sin\theta\sin\theta'\cos\left(\lambda' - \lambda\right). \tag{4}$$

Applying the additional theorem, the Legendre polynomials P_n are expressed in terms of the (fully normalized) Legendre associated functions $\bar{P}_{nm}$ in the following form:

$$P_n\left(\cos\psi\right) = \frac{1}{2n+1} \sum_{m=0}^{n} \bar{P}_{nm}\left(\cos\theta\right)\bar{P}_{nm}\left(\cos\theta'\right) \times \left(\cos m\lambda\cos m\lambda' + \sin m\lambda\sin m\lambda'\right). \tag{5}$$

We further define the (fully normalized) surface spherical harmonic functions Y_{nm}^{α} of degree n and order m by (e.g., Colombo, 1981)

$$Y_{nm}^{\alpha}\left(\theta,\lambda\right) = \bar{P}_{nm}\left(\cos\theta\right)\begin{cases}\cos m\lambda & \text{when } \alpha = 0 \\ \sin m\lambda & \text{when } \alpha = 1\end{cases}. \tag{6}$$

Substituting from Equation 6 to Equation 5, we arrive at

$$P_n\left(\cos\psi\right) = \frac{1}{2n+1} \sum_{m=0}^{n} \sum_{\alpha=0}^{1} Y_{nm}^{\alpha}\left(\theta,\lambda\right)Y_{nm}^{\alpha}\left(\theta',\lambda'\right). \tag{7}$$

Combining Equations 1, 3 and 7, we get

$$\begin{aligned}&\delta T(r,\theta,\lambda)\\&= G(R - D_0)^2 \iint_{\sigma} \kappa(\theta',\lambda') \sum_{n=0}^{\infty} \frac{(R - D_0)^n}{r^{n+1}} \frac{1}{2n+1} \sum_{m=0}^{n} \sum_{\alpha=0}^{1} Y_{nm}^{\alpha}(\theta,\lambda)Y_{nm}^{\alpha}(\theta',\lambda')d\sigma\\&= G(R - D_0)^2 \sum_{n=0}^{\infty} \frac{(R - D_0)^n}{r^{n+1}} \frac{1}{2n+1} \sum_{m=0}^{n} \sum_{\alpha=0}^{1} Y_{nm}^{\alpha}(\theta,\lambda)\iint_{\sigma} \kappa(\theta',\lambda')Y_{nm}^{\alpha}(\theta',\lambda')d\sigma.\end{aligned} \tag{8}$$

We apply a spherical harmonic analysis to define $\kappa\left(\theta,\lambda\right)$ in terms of their spherical harmonics. We write

$$\kappa_{nm}^{\alpha} = \frac{1}{4\pi} \iint_{\sigma} \kappa\left(\theta',\lambda'\right)Y_{nm}^{\alpha}\left(\theta',\lambda'\right)d\sigma. \tag{9}$$

The substitution from Equation 9 back to Equation 8 yields

$$\delta T\left(r,\theta,\lambda\right) = 4\pi G\left(R - D_0\right)^2 \sum_{n=0}^{\infty} \frac{\left(R - D_0\right)^n}{r^{n+1}} \frac{1}{2n+1} \sum_{m=0}^{n} \sum_{\alpha=0}^{1} \kappa_{nm}^{\alpha}Y_{nm}^{\alpha}\left(\theta,\lambda\right). \tag{10}$$

We further scale the expression in Equation 10 by the geocentric gravitational constant *GM* that is defined by

$$GM = \frac{4}{3}\pi R^3 \rho_E. \tag{11}$$

From Equations 11 and 10, we get

$$\delta T\left(r,\theta,\lambda\right) = \frac{GM}{R}\sum_{n=0}^{\infty}\frac{R^{n+1}}{r^{n+1}}\sum_{m=0}^{n}\sum_{\alpha=0}^{1}Y_{nm}^{\alpha}\left(\theta,\lambda\right)\Delta V_{nm}^{\alpha}, \tag{12}$$

where

$$\Delta V_{nm}^{\alpha} = \frac{3\kappa_{nm}^{\alpha}}{\left(2n+1\right)\rho_E\left(R-D_0\right)}\left(\frac{R-D_0}{R}\right)^{n+3}. \tag{13}$$

From Equation 13, we define the spherical harmonic coefficients of surface density anomalies as follows:

$$\kappa_{nm}^{\alpha} = \frac{\left(2n+1\right)\rho_E\left(R-D_0\right)}{3}\left(\frac{R}{R-D_0}\right)^{n+3}\Delta V_{nm}^{\alpha}. \tag{14}$$

The application of spherical harmonic synthesis in Equation 14 yields

$$\kappa\left(\theta,\lambda\right) = \sum_{n=0}^{\infty}\sum_{m=0}^{n}\sum_{\alpha=0}^{1}\kappa_{nm}^{\alpha}Y_{nm}^{\alpha}\left(\theta,\lambda\right). \tag{15}$$

Now we introduce the Moho depth as a function of surface density anomalies. From Equations 2 and 15, we write

$$D\left(\theta,\lambda\right) = D_0 + \frac{\kappa\left(\theta,\lambda\right)}{\Delta\rho\left(\theta,\lambda\right)}, \tag{16}$$

where $\Delta\rho$ is a variable Moho density contrast.

If $\Delta\rho$ = const., Equation 16 reduces to

$$D\left(\theta,\lambda\right) = D_0 + \frac{\kappa\left(\theta,\lambda\right)}{\Delta\rho}. \tag{17}$$

The expression in Equation 14 defines a functional relation between the spherical harmonic coefficients of the surface density anomaly and the disturbing potential (Chen et al., 2018). A similar spectral expression for a Moho depth recovery from the disturbing potential coefficients was derived before by Reguzzoni et al. (2013). The expressions for a Moho modeling from the GOCE gravity gradient data were derived in Reguzzoni and Sampietro (2015) and Eshagh and Hussain (2016).

In the next section, we derive the expressions for gravity and gravity gradient data in spatial and spectral forms. We note that the expressions derived in the spatial form are suitable for a regional gravimetric Moho recovery. As mentioned above, the developed algorithm is numerically very efficient. The reason is that the algorithm is based on a linear relation between gravity (or gravity gradient) and density changes.

To begin with, we first define the gravity disturbance as a negative radial derivative of the disturbing potential generated by the Moho depth undulations, that is,

$$\delta g = -\frac{\partial \delta T}{\partial r}. \tag{18}$$

Inserting from Equation 18 to Equation 12, we get

$$\delta g\left(r,\theta,\lambda\right) = \frac{GM}{R^2} \sum_{n=0}^{\infty} \left(\frac{R}{r}\right)^{n+2} \left(n+1\right) \sum_{m=0}^{n} \sum_{\alpha=0}^{1} Y_{nm}^{\alpha}\left(\theta,\lambda\right) \Delta V_{nm}^{\alpha}. \tag{19}$$

The combination of Equations 13 and 19 yields

$$\left(\frac{\delta g R^2}{GM}\right)_{nm}^{\alpha} = \frac{3\left(n+1\right)\kappa_{nm}^{\alpha}}{R\left(2n+1\right)\rho_E} \left(\frac{R-D_0}{r}\right)^{n+2}. \tag{20}$$

After some algebra, we arrive at

$$\kappa_{nm}^{\alpha} = \left(\frac{\delta g R^2}{GM}\right)_{nm}^{\alpha} \frac{\left(2n+1\right)R\rho_E}{3\left(n+1\right)} \left(\frac{r}{R-D_0}\right)^{n+2}. \tag{21}$$

We further simplify Equation 21 as follows:

$$\kappa_{nm}^{\alpha} = \delta g_{nm}^{\alpha} \frac{\left(2n+1\right)}{4\pi\left(n+1\right)} \left(\frac{r}{R-D_0}\right)^{n+2}. \tag{22}$$

The expression in Equation 22 defines the relationship between spherical harmonics of surface density anomalies and spherical harmonics of gravity disturbances.

By analogy with Equation 18, we define the expression for a Moho depth recovery from gravity gradiometry data. We first define the vertical gravity gradient by

$$\delta\Gamma_{rr} = \frac{\partial^2 \delta T}{\partial r^2}. \tag{23}$$

Substituting from Equation 12 to Equation 23, we arrive at

$$\delta\Gamma_{rr}\left(r,\theta,\lambda\right) = \frac{GM}{R^3} \sum_{n=0}^{\infty} \left(\frac{R}{r}\right)^{n+3} \left(n+1\right)\left(n+2\right) \sum_{m=0}^{n} \sum_{\alpha=0}^{1} Y_{nm}^{\alpha}\left(\theta,\lambda\right) \Delta V_{nm}^{\alpha}. \tag{24}$$

The combination of Equations 13 and 24 yields

$$\left(\frac{\delta\Gamma_{rr} R^3}{GM}\right)_{nm}^{\alpha} = \left(n+1\right)\left(n+2\right) \frac{3\kappa_{nm}^{\alpha}}{\left(2n+1\right)\rho_E\left(R-D_0\right)} \left(\frac{R-D_0}{r}\right)^{n+2}, \tag{25}$$

where

$$\kappa_{nm}^{\alpha} = \left(\frac{\delta\Gamma_{rr} R^3}{GM}\right)_{nm}^{\alpha} \frac{\left(2n+1\right)\rho_E\left(R-D_0\right)}{3\left(n+1\right)\left(n+2\right)} \left(\frac{r}{R-D_0}\right)^{n+3}. \tag{26}$$

Finally, we simplify the expression in Equation 26 as follows:

$$\kappa_{nm}^{\alpha} = \left(\frac{\delta\Gamma_{rr}}{GM}\right)_{nm}^{\alpha} \frac{\left(2n+1\right)\left(R-D_0\right)}{\left(n+1\right)\left(n+2\right)} \left(\frac{r}{R-D_0}\right)^{n+3}. \tag{27}$$

The expressions in Equations 22 and 27 define (linear) functional models for a Moho recovery from gravity and gravity gradiometry data, respectively, in the spectral domain. The corresponding expressions in the spatial domain are derived next.

2.2. Functional Models in Spatial Domain

Applying spherical harmonic synthesis on both sides of Equation 13, we get

$$\sum_{n=0}^{\infty}\sum_{m=0}^{n}\sum_{\alpha=0}^{1}\Delta V_{nm}^{\alpha}Y_{nm}^{\alpha}\left(\theta,\lambda\right) = \sum_{n=0}^{\infty}\sum_{m=0}^{n}\sum_{\alpha=0}^{1}\frac{3\kappa_{nm}^{\alpha}}{\left(2n+1\right)\rho_{E}\left(R-D_{0}\right)}\left(\frac{R-D_{0}}{R}\right)^{n+3}Y_{nm}^{\alpha}\left(\theta,\lambda\right). \tag{28}$$

We further rearrange Equation 28 into the following form:

$$\Delta V\left(\theta,\lambda\right) = \sum_{n=0}^{\infty}\sum_{m=0}^{n}\sum_{\alpha=0}^{1}\frac{3\kappa_{nm}^{\alpha}}{\left(2n+1\right)\rho_{E}\left(R-D_{0}\right)}\left(\frac{R-D_{0}}{R}\right)^{n+3}Y_{nm}^{\alpha}\left(\theta,\lambda\right)$$
$$= \sum_{n=0}^{\infty}\frac{3\kappa_{n}\left(\theta,\lambda\right)}{\left(2n+1\right)\rho_{E}\left(R-D_{0}\right)}\left(\frac{R-D_{0}}{R}\right)^{n+3}, \tag{29}$$

where $\kappa_{n}\left(\theta,\lambda\right)$ is defined by (e.g., Heiskanen & Moritz, 1967)

$$\kappa_{n}\left(\theta,\lambda\right) = \frac{2n+1}{4\pi}\iint_{\sigma}\kappa\left(\theta',\lambda'\right)P_{n}\left(\cos\psi\right)d\sigma. \tag{30}$$

The substitution from Equation 29 to Equation 30 yields

$$\Delta V\left(\theta,\lambda\right) = \sum_{n=0}^{\infty}\frac{3}{\left(2n+1\right)\rho_{E}\left(R-D_{0}\right)}\left(\frac{R-D_{0}}{R}\right)^{n+3}\frac{2n+1}{4\pi}\iint_{\sigma}\kappa\left(\theta',\lambda'\right)P_{n}\left(\cos\psi\right)d\sigma$$
$$= \frac{3}{4\pi\rho_{E}\left(R-D_{0}\right)}\sum_{n=0}^{\infty}\left(\frac{R-D_{0}}{R}\right)^{n+3}\iint_{\sigma}\kappa\left(\theta',\lambda'\right)P_{n}\left(\cos\psi\right)d\sigma. \tag{31}$$

Introducing the parameter $\tau = \left(R-D_{0}\right)/R$, the expression in Equation 31 becomes

$$\Delta V\left(\theta,\lambda\right) = \frac{3}{4\pi\rho_{E}\left(R-D_{0}\right)}\sum_{n=0}^{\infty}\tau^{n+3}\iint_{\sigma}\kappa\left(\theta',\lambda'\right)P_{n}\left(\cos\psi\right)d\sigma$$
$$= \frac{3}{4\pi\rho_{E}\left(R-D_{0}\right)}\iint_{\sigma}\kappa\left(\theta',\lambda'\right)\left\{\sum_{n=0}^{\infty}\tau^{n+3}P_{n}\left(\cos\psi\right)\right\}d\sigma. \tag{32}$$

From Equation 32, we define the surface integral kernel S as follows:

$$S\left(\psi\right) = \sum_{n=0}^{\infty}\tau^{n+3}P_{n}\left(\cos\psi\right) = \tau^{3}\sum_{n=0}^{\infty}\tau^{n}P_{n}\left(\cos\psi\right). \tag{33}$$

We further write the following identity:

$$\sum_{n=0}^{\infty}\tau^{n}P_{n}\left(\cos\psi\right) = \frac{1}{\sqrt{1+\tau^{2}-2\tau\cos\psi}}. \tag{34}$$

Combining Equations 33 and 34, the closed form of the kernel function S is found to be

$$S_{V}\left(\psi\right) = \tau^{3}\sum_{n=0}^{\infty}\tau^{n}P_{n}\left(\cos\psi\right) = \frac{\tau^{3}}{\sqrt{1+\tau^{2}-2\tau\cos\psi}}. \tag{35}$$

Inserting from Equation 35 back to Equation 32, the relationship between the disturbing potential and the surface density anomalies is obtained. It reads

$$\Delta V\left(\theta,\lambda\right) = \frac{3}{4\pi\rho_{E}\left(R-D_{0}\right)}\iint_{\sigma}\kappa\left(\theta',\lambda'\right)S_{V}\left(\psi\right)d\sigma. \tag{36}$$

Applying spherical harmonic synthesis on both sides of Equation 20, we arrive at

$$\sum_{n=0}^{\infty}\sum_{m=0}^{n}\sum_{\alpha=0}^{1}\left(\frac{\delta g R^2}{GM}\right)_{nm}^{\alpha} Y_{nm}^{\alpha}(\theta,\lambda) = \sum_{n=0}^{\infty}\sum_{m=0}^{n}\sum_{\alpha=0}^{1}\frac{3(n+1)\kappa_{nm}^{\alpha}}{(2n+1)R\rho_E}\left(\frac{R-D_0}{r}\right)^{n+2} Y_{nm}^{\alpha}(\theta,\lambda). \tag{37}$$

From Equation 37, we further write

$$\begin{aligned}\frac{R^2}{GM}\delta g(\theta,\lambda) &= \sum_{n=0}^{\infty}\sum_{m=0}^{n}\sum_{\alpha=0}^{1}\frac{3(n+1)\kappa_{nm}^{\alpha}}{(2n+1)R\rho_E}\left(\frac{R-D_0}{r}\right)^{n+2} Y_{nm}^{\alpha}(\theta,\lambda)\\ &= \frac{3}{R\rho_E}\sum_{n=0}^{\infty}\frac{(n+1)}{(2n+1)}\left(\frac{R-D_0}{r}\right)^{n+2}\kappa_n(\theta,\lambda).\end{aligned} \tag{38}$$

Combining Equations 30 and 38, we get

$$\frac{R^2}{GM}\delta g(\theta,\lambda) = \frac{3}{R\rho_E}\sum_{n=0}^{\infty}\frac{(n+1)}{(2n+1)}\left(\frac{R-D_0}{r}\right)^{n+2}\frac{2n+1}{4\pi}\iint_{\sigma}\kappa(\theta',\lambda')P_n(\cos\psi)d\sigma. \tag{39}$$

Consequently,

$$\delta g(\theta,\lambda) = G\sum_{n=0}^{\infty}(n+1)\left(\frac{R-D_0}{r}\right)^{n+2}\iint_{\sigma}\kappa(\theta',\lambda')P_n(\cos\psi)d\sigma. \tag{40}$$

Introducing the parameter $\tau_1 = (R-D_0)/r$, we write

$$\delta g(\theta,\lambda) = G\iint_{\sigma}\kappa(\theta',\lambda')\sum_{n=0}^{\infty}(n+1)\tau_1^{n+2}P_n(\cos\psi)d\sigma. \tag{41}$$

We further define the integral kernel S_g by

$$S_g(\psi) = \sum_{n=0}^{\infty}(n+1)\tau_1^{n+2}P_n(\cos\psi) = \tau_1^2\sum_{n=0}^{\infty}n\tau_1^n P_n(\cos\psi) + \tau_1^2\sum_{n=0}^{\infty}\tau_1^n P_n(\cos\psi). \tag{42}$$

By analogy with Equation 34, we get

$$\sum_{n=0}^{\infty}\tau_1^n P_n(\cos\psi) = \frac{1}{\sqrt{1+\tau_1^2-2\tau_1\cos\psi}}. \tag{43}$$

The first derivative of the expression in Equation 43 with respect to τ_1 reads

$$\begin{aligned}\sum_{n=0}^{\infty}n\tau_1^n P_n(\cos\psi) &= -\frac{1}{2}\left(1+\tau_1^2-2\tau_1\cos\psi\right)^{-3/2}\left(2\tau_1-2\cos\psi\right)\\ &= -\tau_1\left(\tau_1-\cos\psi\right)\left(1+\tau_1^2-2\tau_1\cos\psi\right)^{-3/2}.\end{aligned} \tag{44}$$

Inserting from Equations 43 and 44 back to Equation 42, the closed form of S_g is found to be

$$S_g(\psi) = \frac{\tau_1^2 - \tau_1^3\cos\psi}{\left(1+\tau_1^2-2\tau_1\cos\psi\right)\sqrt{1+\tau_1^2-2\tau_1\cos\psi}}. \tag{45}$$

The spatial expression for a Moho recovery from gravity data then reads

$$\delta g(\theta,\lambda) = G\iint_{\sigma}\kappa(\theta',\lambda')S_g(\psi)d\sigma. \tag{46}$$

Applying spherical harmonic synthesis on both sides of Equation 25, that is,

$$\sum_{n=0}^{\infty} \sum_{m=0}^{n} \sum_{\alpha=0}^{1} \left(\frac{\delta\Gamma_{rr}R^3}{GM} \right)_{nm}^{\alpha} Y_{nm}^{\alpha}(\theta,\lambda) = \sum_{n=0}^{\infty} \sum_{m=0}^{n} \sum_{\alpha=0}^{1} (n+1)(n+2) \frac{3\kappa_{nm}^{\alpha}}{(2n+1)\rho_E(R-D_0)} \tag{47}$$

$$\times \left(\frac{R-D_0}{r} \right)^{n+3} Y_{nm}^{\alpha}(\theta,\lambda),$$

and some algebra, we arrive at

$$\delta\Gamma_{rr}(\theta,\lambda) = \frac{3GM}{R^3\rho_E(R-D_0)} \sum_{n=0}^{\infty} \frac{(n+1)(n+2)\kappa_n(\theta,\lambda)}{(2n+1)} \left(\frac{R-D_0}{r} \right)^{n+3}. \tag{48}$$

Combining Equations 30 and 48, we get

$$\delta\Gamma_{rr}(\theta,\lambda) = \frac{3GM}{4\pi R^3\rho_E(R-D_0)} \sum_{n=0}^{\infty} (n+1)(n+2) \left(\frac{R-D_0}{r} \right)^{n+3} \iint_{\sigma} \kappa(\theta',\lambda') P_n(\cos\psi) d\sigma$$

$$= \frac{G}{(R-D_0)} \iint_{\sigma} \kappa(\theta',\lambda') \left[\sum_{n=0}^{\infty} (n+1)(n+2) \left(\frac{R-D_0}{r} \right)^{n+3} P_n(\cos\psi) \right] d\sigma. \tag{49}$$

From Equation 49 and the definition of $\tau_1 = (R-D_0)/r$, we introduce the integral kernel S_Γ in the following form:

$$S_\Gamma(\psi) = \sum_{n=0}^{\infty} (n+1)(n+2)\tau_1^{n+3} P_n(\cos\psi)$$

$$= \tau_1^3 \sum_{n=0}^{\infty} (n^2 + 3n + 2)\tau_1^n P_n(\cos\psi) \tag{50}$$

$$= \tau_1^3 \sum_{n=0}^{\infty} n^2 \tau_1^n P_n(\cos\psi) + 3\tau_1^3 \sum_{n=0}^{\infty} n\tau_1^n P_n(\cos\psi) + 2\tau_1^3 \sum_{n=0}^{\infty} \tau_1^n P_n(\cos\psi).$$

Moreover, we adopt the following notation:

$$\sum_{n=0}^{\infty} \tau_1^n P_n(\cos\psi) = \frac{1}{\sqrt{1 + \tau_1^2 - 2\tau_1 \cos\psi}} = \frac{1}{\Lambda}. \tag{51}$$

The first derivative of Equation 44 with respect to τ_1 reads

$$\sum_{n=0}^{\infty} n^2 \tau_1^n P_n(\cos\psi) = \frac{\tau_1^2 \left[-\Lambda^2 + 3(\tau_1 - \cos\psi)^2 \right] - \Lambda^2 \tau_1(\tau_1 - \cos\psi)}{\Lambda^5}. \tag{52}$$

Combining Equations 44, 51 and 52, the kernel function S_Γ is obtained in the following closed form:

$$S_\Gamma(\psi) = \tau_1^3 \frac{2\Lambda^4 - 5\tau_1^2\Lambda^2 + 3\tau_1^2(\tau_1 - \cos\psi)^2] + 4\Lambda^2\tau_1 \cos\psi}{\Lambda^5}. \tag{53}$$

The relationship between the gravity gradient and the surface density anomalies is then described by

$$\delta\Gamma_{rr}(\theta,\lambda) = \frac{G}{(R-D_0)} \iint_{\sigma} \kappa(\theta',\lambda') S_\Gamma(\psi) d\sigma. \tag{54}$$

The surface integral equations (for gravity and gravity gradient data) in Equations 46 and 54 are discretized to form a system of linearized observation equations to solve the gravimetric inverse problem for a Moho depth recovery. Using the vector–matrix notation, the system of observation equations is written as

$$\mathbf{Ax} = \mathbf{b} + \boldsymbol{\varepsilon},$$

(55)

where $\mathbf{A}$ is the design matrix, $\mathbf{x}$ is the vector of the unknown surface density anomaly values, $\mathbf{b}$ is the vector of observations (gravity or gravity gradient values), and $\boldsymbol{\varepsilon}$ is the vector of residuals.

The linearized system of observation equations in Equation 55 is ill-conditioned, and it inverse solution is sensitive to a noise from observation data. The Tikhonov's regularization (Phillips, 1962; A. Tikhonov, 1963; A. N. Tikhonov & Arsenin, 1977) is often applied to stabilize an inversion procedure. The principle is to define the regularization solution $\mathbf{X}_\lambda$ that minimizes the following weighted combination of the residual norm and the side constraint:

$$\mathbf{X}_{\text{\tiny{\textsl{»}}}} = \text{argmin}\left\{\left\|\mathbf{Ax} - \mathbf{b}\right\|_2^2 + \lambda^2 \left\|\mathbf{Ix}\right\|_2^2\right\},$$

(56)

where $\mathbf{I}$ is the identity matrix, and λ is a regularization parameter. We applied the generalized cross-validation to find the optimal regularization parameter.

Combining Equations 55 and 56, the solution for $\mathbf{x}$ reads

$$\mathbf{X}_\lambda = \left(\mathbf{A}^\mathbf{T}\mathbf{A} + \lambda^2\mathbf{I}\right)^{-1}\mathbf{A}^\mathbf{T}\mathbf{b},$$

(57)

where $\mathbf{X}_\lambda$ is a regularized solution which can reduce noise from input data.

3. Numerical Realization

We applied numerical models in the spatial form to estimate the Moho depth in Tibet. Input data acquisition and computational procedures are summarized next.

3.1. Input Data Acquisition

We computed the (free-air) gravity disturbances and the corresponding (radial) gravity gradient values from the satellite gravitational model GOCO06S (Kvas et al., 2019) with a spectral resolution up to degree/order of 180 after removing the GRS80 (Moritz, 2000) normal gravity and gravity gradient components, respectively. We then applied the tesseroid method (Asgharzadeh et al., 2007; Grombein et al., 2013; Wild-Pfeiffer, 2008) to compute the topographic and stripping corrections (to gravity and gravity gradient) due to bathymetry, sediments, and consolidated (crystalline) crust. The topographic and bathymetric gravity and gravity gradient corrections were computed from the ETOPO1 (Amante & Eakins, 2009) topographic/bathymetric data. The density and thickness data of sediments and consolidated curst were retrieved from the CRUST1.0 global seismic crustal model (Laske et al., 2013). It is worth mentioning that a spectral resolution up to degree of 180 corresponds to a spatial resolution of about 1° (in terms of a half wavelength) or about 110 km (on equator) used in this study to compute gravity field quantities and to estimate the Moho depth is adequate for a gravimetric Moho modeling. Turcotte and Schubert (2014, p. 252) acquired that the spatial resolution of about 100 km represents a limit below which loads are not compensated. In other words, the gravimetric determination of more detailed features in the Moho geometry might not be realistic. A more detailed regional modeling of the Moho depth from gravity data is possible only if there is enough seismic Moho estimates to constrain the gravimetric result.

We adopted the upper continental crustal density of 2,670 kg/m^3 (cf., Hinze, 2003) to compute the topographic correction. To compute the bathymetric correction, we used a seawater density–depth equation (Gladkikh & Tenzer, 2012) which is more accurate than a uniform density model (cf., Tenzer, Novák, et al., 2012; Tenzer, Pavel, et al., 2012; Tenzer et al., 2010, 2011). We then used the CRUST1.0 sediment and
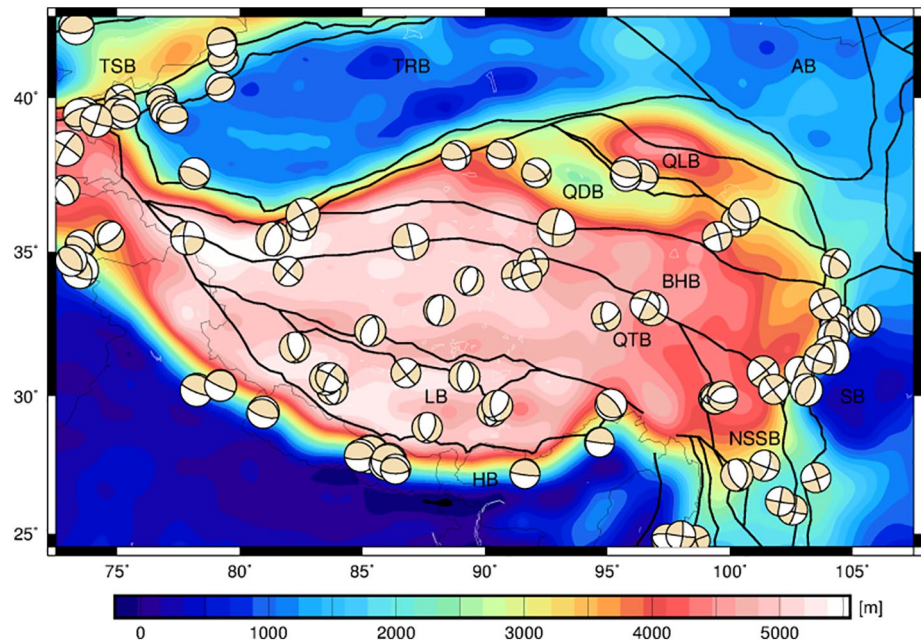
Figure 1. Topography and tectonic setting of the study area. Abbreviations used: Sichuan Basin (SB), Northwest Sichuan Subblock (NSSB), Bayan Hara Block (BHB), Alashan Block (AB), Qaidam Basin (QDB), Lhasa Block (LB), Tarim Block (TRB), Himalayan Block (HB), Qilian Block (QLB), Qiangtang Block (QTB), and Tian Shan Block (TSB). Yellow beach balls indicate locations of large earthquakes occurring between 1976 and 2019 with magnitude exceeding 6.0 (on Richter's scale) (see website: https://www.globalcmt.org).

consolidated crustal density and thickness data to compute the sediment and consolidated crust gravity and gravity gradient corrections. To realistically simulate a gravimetric Moho recovery from satellite-derived gravitational models, all computations were realized on a 1° × 1° grid of spherical coordinates at satellite elevation of 250 km within the data area that extends the study area by 5° in each direction. The topography and tectonic setting of the study area are shown in Figure 1.

We applied the computed gravity corrections to the free-air gravity disturbances. By analogy, we applied the corresponding gravity gradient corrections to values of the vertical gravity gradient. In addition, we subtracted also a long-wavelength part of gravity and gravity gradient spectra up to degree 17 of spherical harmonics in order to suppress a signature of density heterogeneities within the lower mantle (e.g., Bowin, 2000). This spherical harmonic degree was selected based on a principle of minimizing a bias between the gravimetric and seismic (CRUST1.0) Moho depths. The Bouguer gravity disturbances and gravity gradient values obtained after applying these procedures are shown in Figure 2. We note that regional maps of individual gravity and gravity gradient corrections as well as intermediate results obtained after applying these corrections to observed gravity disturbances and vertical gravity gradient values are not presented here. Tenzer and Chen (2019) presented and interpreted globally these gravity corrections and step-wise corrected gravity disturbances, and Novák and Tenzer (2013) conducted a similar study for the gravity gradient.

We see a similar spatial pattern in both the Bouguer gravity and gravity gradient maps. Maximum negative values of the Bouguer gravity disturbances and gravity gradients are detected over Tibet and Himalayas. Small negative values (and partially also small positive gravity gradients) are seen over continental basins (Tarim, Sichuan, and Ganga) as well as over the Alashan Block. This prevailing spatial pattern confirms a high (negative) correlation between both gravity field quantities and a Moho geometry that is dominated by an isostatic signature of mountains and elevated plateau. This isostatic signature is obviously characterized by large negative values of the Bouguer gravity disturbances and gravity gradient. In contrast, lowlands and continental basins are characterized by small, typically negative values.
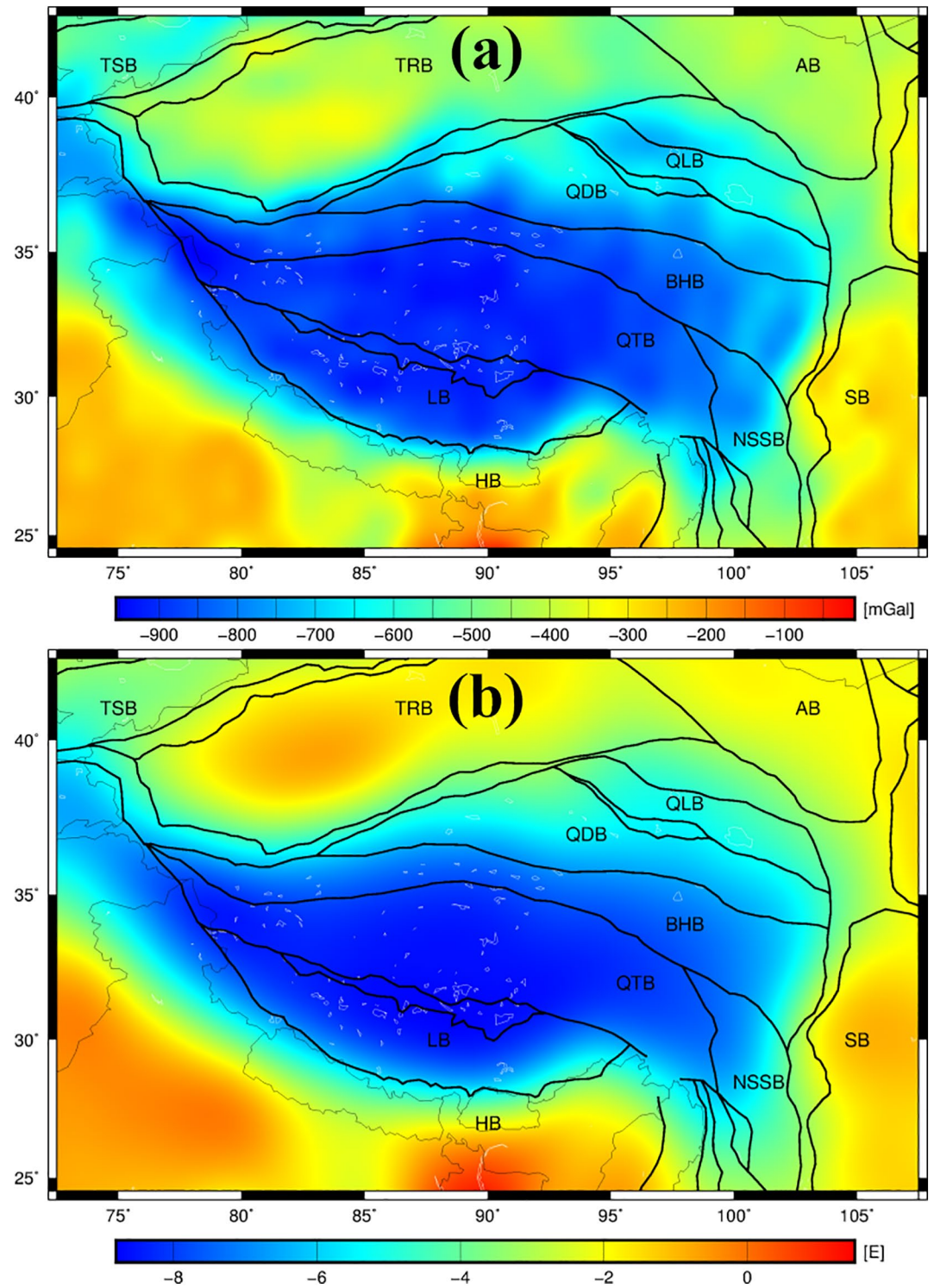
Figure 2. Regional maps of (a) Bouguer gravity disturbances (statistics: min, −947 mGal; max, −59 mGal; mean, −553 mGal; standard deviation STD, 223 mGal) and (b) Bouguer gravity gradients (statistics: min, −8.6 E; max, 1.1 E; mean, −3.9 E; STD, 2.6 E).
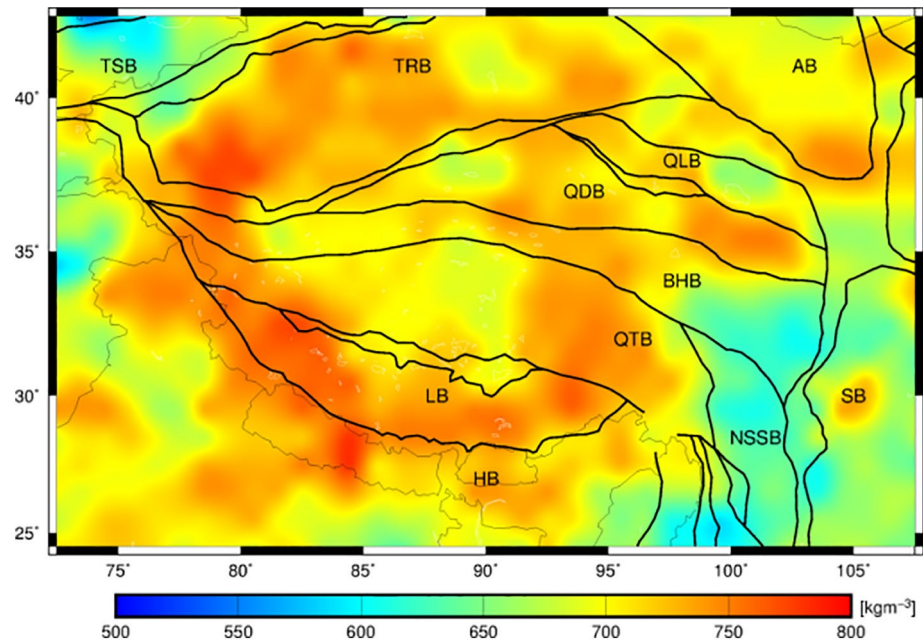
Figure 3. Moho density contrast computed as the difference between the CRUST1.0 uppermost mantle density and the reference crustal density (statistics: min, 560 kg/m³; max, 780 kg/m³; mean, 701 kg/m³; STD, 37 kg/m³).

3.2. Moho Parameters

Since a Moho depth recovery from the gravity (or gravity gradiometry) data is a nonunique problem, some a priori assumptions are required to solve this problem, particularly by selecting a mean Moho depth and the Moho density contrast. In our approach, we used the mean Moho depth of 50.6 km. This value was obtained as the average Moho depth within the study area based on the CRUST1.0 model. For the constant Moho density contrast, different values can be used. Dziewonski and Anderson (1981) adopted a constant value of 480 kg/m³ in the Preliminary Reference Earth Model. Sjöberg and Bagherbandi (2011) estimated that the global average Moho density contrast is 448 ± 187 kg/m³. They also provided individual estimates for the continental crust of 678 ± 78 kg/m³ and for the oceanic crust of 334 ± 108 kg/m³. The estimated value of 485 kg/m³ by Tenzer, Novák, et al. (2012) and Tenzer, Pavel, et al. (2012) was later updated to 445 kg/m³ (cf., Tenzer et al., 2015) based on applying more advanced methods and using more recent data sets. We adopted this value to define the uniform Moho density contrast. We also adopted this density value for the crust in definition of the variable Moho density contrast and used the uppermost mantle density data from the CRUST1.0 global seismic model. We note that by removing low-degree spherical harmonics (up to degree 17) from gravity and gravity gradient spectra, we mainly removed a signature of density heterogeneities within the lower mantle, while a gravitational signature of more localized density heterogeneities within the uppermost mantle (including a Moho geometry) is still present at a medium-to-higher frequency of gravity and gravity gradient spectra. The variable Moho density contrast is shown in Figure 3. Within the study area, these density contrast variations are within 560–780 kg/m³.

We used the Bouguer gravity disturbances and gravity gradient values computed (on a 1° × 1° grid at satellite elevation of 250 km) within the data area to estimate the Moho depth (on a 1° × 1° grid) within the study area of Tibet. The results were obtained by solving the system of normal equations with regularization in Equation 57.

4. Results

Results of a Moho recovery from the Bouguer gravity disturbances and gravity gradient values for the uniform and variable Moho density contrasts are presented in Figure 4. All four gravimetric Moho solutions have a similar spatial pattern. Nevertheless, we also see some significant regional differences between them.
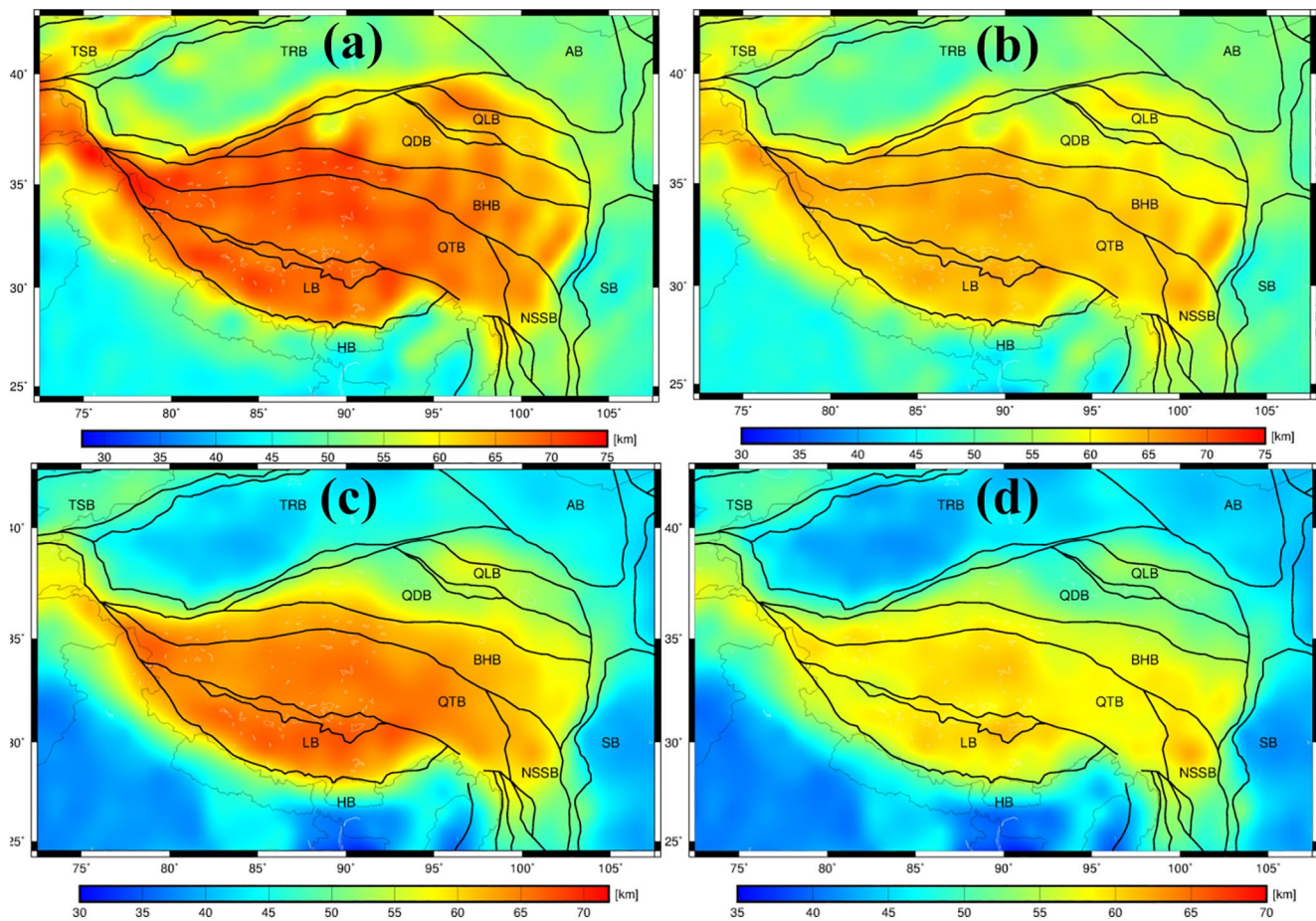
Figure 4. Gravimetric Moho depth solutions computed from the Bouguer gravity disturbances for (a) the uniform and (b) variable Moho density contrasts. The corresponding solutions obtained from the Bouguer gravity gradient values for the uniform and variable Moho density contrasts are shown in (c) and (d), respectively.

This is particularly evident from deeper Moho estimates beneath central Tibet and Himalaya when disregarding density contrast variations at the Moho interface. To inspect these differences, we compared these four gravimetric results with existing seismic and gravimetric models.

We used the two seismic and two gravimetric Moho models (see Figure 5 and statistics in Table 1) to validate our results obtained by applying our algorithm (shown in Figure 4). In particular, we used the Moho depth from the CRUST1.0 seismic global model. We then used the regional seismic Moho model prepared by Li et al. (2014). We also compared our results with the gravimetric results obtained by applying the VMM and Parker–Oldenburg's methods. For this purpose, we applied the Parker–Oldenburg's method to compute the Moho depth and used the same input gravity data and parameters (i.e., the mean Moho depth and the constant Moho density contrast) as for the computation of our gravimetric result (for the uniform Moho density contrast). The VMM gravimetric Moho depth model was prepared by Bagherbandi (2012). The Moho depth differences between gravimetric and seismic results are plotted in Figure 6; for their statistical summary see Table 2.

From the comparison of results in Figures 4 and 5, we see that all our four regional gravimetric solutions (Figure 4) exhibit a spatial pattern that is generally consistent with the regional seismic Moho model prepared by Li et al. (2014) (Figure 5b). In contrast, the CRUST1.0 seismic and regional gravimetric solutions computed by applying the VMM (Bagherbandi, 2012) and Parker–Oldenburg's methods (Figures 5a, 5c, and 5d) exhibit much more complex spatial variations in the Moho depth. This is most evident by the existence of two or more localized maxima of the Moho deepening in these three results located in Hindu Kush and central Himalaya.
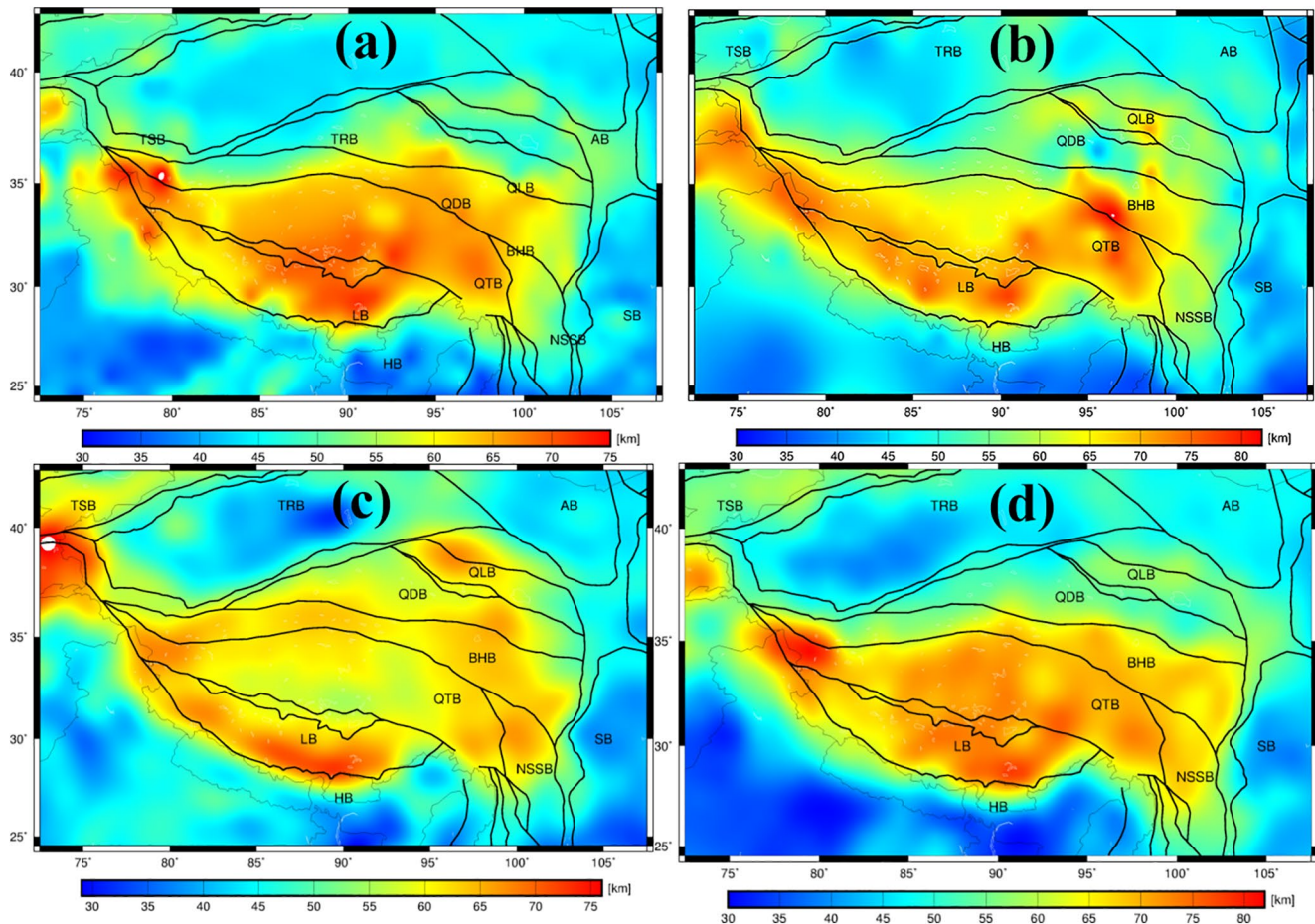
Figure 5. Moho models used for the validation: (a) CRUST1.0 global seismic model, (b) regional seismic model prepared by Li et al. (2014), (c) regional gravimetric model based on applying the Parker–Oldenburg's method, and (d) regional gravimetric model prepared by Bagherbandi (2012) based on solving the VMM inverse problem. VMM, Vening Meinesz–Moritz.

5. Discussion

As seen in Table 2, the gravimetric results obtained by applying our algorithm very closely agree with the CRUST1.0 model by means of a bias. This is particularly evident for the results obtained from the Bouguer gravity disturbances (with a minimum bias), while the corresponding results obtained from the Bouguer gravity gradients are slightly biased. This is explained by the fact that we computed the mean Moho depth parameter by averaging from CRUST1.0 data. The same applies for the gravimetric results computed by applying the VMM and Parker–Oldenburg's methods. All these regional gravimetric solutions are, however, slightly biased when compared with the regional seismic model prepared by Li et al. (2014). In this case, the most biased is the result obtained from the Bouguer gravity gradient data based on applying our algorithm. This finding is explained by the fact that a gravity gradient inversion has a more localized support. A far-zone contribution typically affects more results from a gravity gradient rather than gravity inversion. Nevertheless, a similar bias is also found for the VMM result from the Bouguer gravity disturbances.

We observe much more significant inconsistencies between the gravimetric and seismic results. The Moho depth differences locally reach or even exceed 20 km. These large differences exist also between individual regional gravimetric solutions. These large differences are obviously reflected also in the RMS of Moho depth differences (Table 2). All four regional gravimetric solutions computed from the Bouguer gravity disturbances (i.e., based on applying the VMM and Parker–Oldenburg's methods as well as our algorithm) closely agree with the regional seismic model prepared by Li et al. (2014). These gravimetric results have also a very similar agreement with the CRUST1.0 global seismic model. When comparing the RMS fit of

Table 1
Statistics of the Moho Depth Results

Moho depth	Min (km)	Max (km)	Mean (km)	STD (km)
$D_{CRUST1.0}$	33.3	74.8	50.6	9.2
$D_{Seismic}$	32.5	82.0	53.3	10.2
D_{PO}	29.7	75.4	51.5	9.3
D_{VMM}	34.8	80.2	50.3	10.6
$D_{uniform}$	34.5	73.5	50.5	8.8
$D_{variable}$	35.4	70.5	50.6	6.2
$D^{\Gamma}_{uniform}$	31.5	70.6	50.2	9.3
$D^{\Gamma}_{variable}$	36.2	68.2	49.4	6.4

Note. Notation used: $D_{CRUST1.0}$ is CRUST1.0 Moho depth; $D_{Seismic}$ is the seismic Moho depth provided by Li et al. (2014); D_{PO} is the gravimetric Moho depth obtained by applying the Parker–Oldenburg's method; D_{VMM} is the gravimetric depth obtained by applying VMM method; $D_{uniform}$ and $D_{variable}$ are Moho depth estimates from the Bouguer gravity disturbances (for the uniform and variable Moho density contrasts) by applying our algorithm; and $D^{\Gamma}_{uniform}$ and $D^{\Gamma}_{variable}$ are the corresponding Moho depth estimates from the Bouguer gravity gradient values (for the uniform and variable Moho density contrasts), respectively.

our gravimetric results obtained by applying our algorithm with respect to both seismic models, we see that the results computed for the variable Moho density contrast are slightly worse than those obtained for the uniform Moho density contrast. This could be explained by uncertainties in the CRUST1.0 uppermost density data that propagate to uncertainties of the variable Moho density contrast values used for the computation of this regional gravimetric model.

Despite some relatively large regional differences found in presented results, these inconsistencies between gravimetric and seismic models are not unexpected when taking into consideration uncertainties in seismic and gravimetric Moho models (e.g., Knapmeyer-Endrun et al., 2014) as well as relatively large Moho depth variations in Tibet and Himalaya. These differences are attributed to several factors. Seismic models are likely to a large extent affected by a relatively low resolution of seismic surveys in this study area. Gravimetric results are, on the other hand, affected by relatively large uncertainties of used lithospheric density models that are determined from limited seismic data in that region. Moreover, another factor that limits availability of a lithospheric density information is the fact that there is not a direct link between seismic wave velocity and mass density. In other words, this factor significantly limits the accuracy of lithospheric density models derived from seismic data and consequently affect the accuracy of estimated Moho depth from gravity data corrected for the gravitational contribution of crustal density structure, while also taking into consideration the lithospheric mantle density information in the variable Moho density contrast.

Interestingly, our algorithm provides the best result when using the Bouguer gravity gradients. As seen in Table 2, this result has the best agreement (by means of the RMS fit) with the regional as well as global seismic Moho models, but only in case of using the uniform Moho density contrast. Surprisingly, possibly large uncertainties in the CRUST1.0 uppermost density data much more significantly affect the gravimetric results obtained from the Bouguer gravity gradients than those obtained from the Bouguer gravity disturbances. A possible explanation is that the results from the Bouguer gravity gradients are more affected by these density uncertainties beneath Tibet. On the contrary, these uncertainties are partially mitigated in the results from the Bouguer gravity disturbances that depend on larger area where these uncertainties are likely smaller than beneath Tibet with a relatively low seismic data coverage.

From these findings, we could conclude that our algorithm for a gravimetric Moho recovery performs similarly as the VMM and Parker–Oldenburg's methods. Our algorithm, however, improves the results when the Bouguer gravity gradients are used as the input data.

6. Summary and Concluding Remarks

Data products obtained from the Earth's satellite observation systems have become indispensable in various geoscience studies that are not limited to only the research of climate, surface processes, hydrosphere, atmosphere, or cryosphere but involve also studies of the Earth's interior as well as geodynamic processes inside the Earth, such as the glacial isostatic adjustment, mantle convection, or global tectonism. In the context of the Earth's inner structure studies, particularly focusing on the Moho geometry and closely related isostatic mechanisms, the gravity information from the satellite missions GRACE and GOCE is the most relevant for these studies together with satellite altimetry products that provide information about the Earth's surface geometry. The main advantage of these data products is their global and homogenous coverage with well-defined stochastic properties. In contrast, seismic data that have been primarily used to investigate the Earth's interior do not yet sufficiently cover large parts of the world. Exploiting possibilities of using satellite data in geoscience studies, we developed a numerically efficient algorithm for a Moho recovery from satellite gravity and gravity gradiometry data.
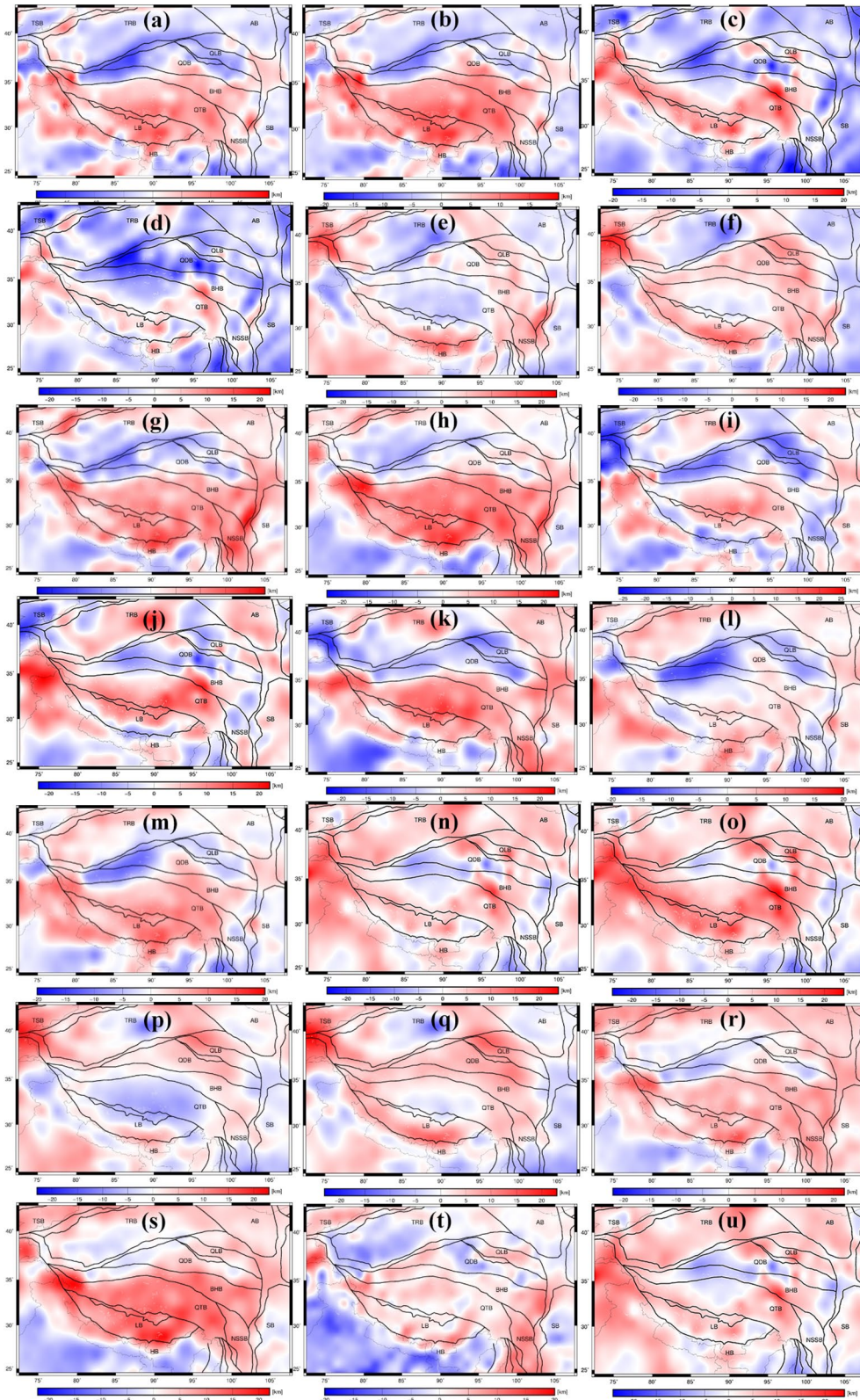
Figure 6. Moho depth differences: (a) $D_{CRUST1.0} - D_{uniform}$, (b) $D_{CRUST1.0} - D_{variable}$, (c) $D_{seismic} - D_{uniform}$, (d) $D_{seismic} - D_{variable}$, (e) $D_{PO} - D_{uniform}$, (f) $D_{PO} - D_{variable}$, (g) $D_{VMM} - D_{uniform}$, (h) $D_{VMM} - D_{variable}$, (i) $D_{CRUST1.0} - D_{PO}$, (j) $D_{seismic} - D_{PO}$, (k) $D_{VMM} - D_{PO}$, (l) $D_{CRUST1.0} - D_{uniform}^{\Gamma}$, (m) $D_{CRUST1.0} - D_{variable}^{\Gamma}$, (n) $D_{seismic} - D_{uniform}^{\Gamma}$, (o) $D_{seismic} - D_{variable}^{\Gamma}$ (p) $D_{PO} - D_{uniform}^{\Gamma}$, (q) $D_{PO} - D_{variable}^{\Gamma}$, (r) $D_{VMM} - D_{uniform}^{\Gamma}$, (s) $D_{VMM} - D_{variable}^{\Gamma}$, (t) $D_{VMM} - D_{CRUST1.0}$, and (u) $D_{VMM} - D_{seismic}$. For notation used, see legend of Table 1.

Table 2
Statistics of the Moho Depth Differences Between Our Four Gravimetric Results (for the Uniform and Variable Moho Density Contrasts and Computed From the Bouguer Gravity and Gravity Gradient Data) and the Four Models Used for the Validation

Moho depth differences	Min (km)	Max (km)	Mean (km)	RMS (km)
$D_{CRUST1.0} - D_{uniform}$	−14.9	16.9	0.1	5.4
$D_{CRUST1.0} - D_{variable}$	−19.1	15.9	0.0	5.5
$D_{seismic} - D_{uniform}$	−19.5	18.5	2.8	6.4
$D_{seismic} - D_{variable}$	−21.8	17.3	2.7	6.5
$D_{PO} - D_{uniform}$	−13.1	17.8	1.0	4.7
$D_{PO} - D_{variable}$	−13.3	20.5	0.9	5.2
$D_{VMM} - D_{uniform}$	−13.3	22.1	−0.2	6.5
$D_{VMM} - D_{variable}$	−12.0	21.7	−0.3	7.0
$D_{CRUST1.0} - D_{PO}$	−25.7	16.7	−0.9	6.5
$D_{seismic} - D_{PO}$	−18.7	21.7	1.8	6.4
$D_{VMM} - D_{PO}$	−19.0	17.2	−1.2	6.9
$D_{CRUST1.0} - D_{uniform}^{\Gamma}$	−15.7	16.4	0.7	4.4
$D_{CRUST1.0} - D_{variable}^{\Gamma}$	−12.2	13.8	1.5	4.8
$D_{seismic} - D_{uniform}^{\Gamma}$	−12.4	23.8	3.1	5.6
$D_{seismic} - D_{variable}^{\Gamma}$	−14.2	23.8	3.8	6.8
$D_{PO} - D_{uniform}^{\Gamma}$	−13.7	20.9	1.3	5.0
$D_{PO} - D_{variable}^{\Gamma}$	−14.8	22.8	2.0	5.4
$D_{VMM} - D_{uniform}^{\Gamma}$	−9.3	14.8	0.1	5.2
$D_{VMM} - D_{variable}^{\Gamma}$	−10.7	21.6	0.9	7.0
$D_{VMM} - D_{CRUST1.0}$	−16.9	15.2	−0.3	5.5
$D_{VMM} - D_{seismic}$	−22.6	13.1	−3.1	6.9

Note. For the notation used, see legend of Table 1.

The developed algorithm utilizes a linear relation between gravity and density by means of defining the Moho depth undulations as a single condensation layer at depth corresponding to a mean Moho depth chosen for a particular study area. We first introduced the relation between the Moho depth undulations and surface density variations, and then converted this functional model to link the Moho depth undulations directly with the Bouguer gravity and gravity gradiometry data.

A commonly used procedure was applied to compute the Bouguer gravity and gravity gradiometry data. This procedure involves the application of corrections to observed gravity and gravity gradiometry data in order to enhance an isostatic signature in the Bouguer gravity and gravity gradient maps. First, the topographic gravity correction was applied to remove the gravitational contribution of topographic masses. The bathymetric, sediment, and consolidated crust gravity corrections were then applied to remove the gravitational contributions of crustal density heterogeneities. To suppress a long-wavelength signal from deep mantle density heterogeneities, we subtracted low-degree spherical harmonics from gravity and gravity gradiometry data. The gravitational contribution of variable density structure within the uppermost mantle, on the other hand, was treated implicitly by considering the variable density contrast at the Moho interface that was computed from the CRUST1.0 uppermost mantle density data and the reference crustal density. The numerical test, however, revealed that such assumption might actually worsen gravimetric results. A possible explanation is that the CRUST1.0 uppermost mantle data are affected by large uncertainties beneath Tibet.

The regional gravimetric results obtained based on applying three different techniques, namely the VMM, Parker–Oldenburg's, and newly developed condensation approaches, have a similar RMS fit with the regional seismic model prepared by Li et al. (2014). All three regional gravimetric results also exhibit a spatial pattern that closely mimics a spatial pattern of this regional seismic model. Our result from the gravity gradient data inversion and for a uniform Moho density contrast has the best RMS fit the regional seismic model as well as a very similar spatial pattern. We speculate that this is possible because our algorithm reduces the influence of far-zone crust density uncertainties, especially when applied for gravity gradient data.

We demonstrated that the developed algorithm provides similar results as the VMM and Parker–Oldenburg's methods. An additional improvement was achieved by applying the developed algorithm for gravity gradient data. This result has the best agreement with tested regional and global seismic Moho models. We explained this by a more localized support of a gravity gradiometry inversion. In this case, however, gravimetric Moho results could be affected more significantly by density errors of lithospheric structure models. It is thus essential to test results for the uniform and variable Moho density contrast models, while also involving existing seismic results for the validation of gravimetric results.

Data Availability Statement

are accessible on the GitHub (https://github.com/wjchennjtech/gravity-and-Moho-data). Figures were prepared using Generic Mapping Tools (Wessel et al., 2013).

References

Aitken, A. R. A., Salmon, M. L., & Kennett, B. L. N. (2013). Australia's Moho: A test of the usefulness of gravity modelling for the determination of Moho depth. *Tectonophysics*, *609*, 468–479.

Amante, C., & Eakins, B. W. (2009). *ETOPO1 1 arc-minute global relief model: Procedures, data sources and analysis*. NOAA Technical Memorandum NESDIS NGDC-24 (19 pp).

Asgharzadeh, M. F., von Frese, R. R. B., Kim, H. R., Leftwich, T. E., & Kim, J. W. (2007). Spherical prism gravity effects by Gauss–Legendre quadrature integration. *Geophysical Journal International*, *169*(1), 1–11. https://doi.org/10.1111/j.1365-246X.2007.03214.x

Bagherbandi, M. (2012). A comparison of three gravity inversion methods for crustal thickness modelling in Tibet plateau. *Journal of Asian Earth Sciences*, *43*(1), 89–97. https://doi.org/10.1016/j.jseaes.2011.08.013

Bassin, C., Laske, G., & Masters, G. (2000). The current limits of resolution for surface wave tomography in North America. *Eos Transactions American Geophysical Union*, *81*(48), F897.

Block, A. E., Bell, R. E., & Studinger, M. (2009). Antarctic crustal thickness from satellite gravity: Implications for the Transantarctic and Gamburtsev Subglacial Mountains. *Earth and Planetary Science Letters*, *288*(1), 194–203.

Bowin, C. (2000). Mass anomaly structure of the Earth. *Reviews of Geophysics*, *38*(3), 355–387.

Braitenberg, C., Pettenati, F., & Zadro, M. (1997). Spectral and classical methods in the evaluation of Moho undulations from gravity data: The NE Italian Alps and isostasy. *Journal of Geodynamics*, *23*(1), 5–22.

Braitenberg, C., Zadro, M., Fang, J., Wang, Y., & Hsu, H. T. (2000). The gravity and isostatic Moho undulations in Qinghai–Tibet plateau. *Journal of Geodynamics*, *30*(5), 489–505.

Chappell, A. R. & Kusznir, N. J. (2008). Three-dimensional gravity inversion for Moho depth at rifted continental margins incorporating a lithosphere thermal gravity anomaly correction. *Geophysical Journal International*, *174*: 1-13.

Chen, W., Tenzer, R., & Li, H. (2018). A regional gravimetric Moho recovery under Tibet using gravitational potential data from a satellite global model. *Studia Geophysica et Geodaetica*, *62*, 624–647.

Colombo, O. L. (1981). *Numerical methods for harmonic analysis on the sphere* (OSU Rep. 310). Department of Geodetic Science and Surveying.

Dziewonski, A. M., & Anderson, D. L. (1981). Preliminary reference Earth model. *Physics of the Earth and Planetary Interiors*, *25*(4), 297–356.

Eshagh, M., & Hussain, M. (2016). An approach to Moho discontinuity recovery from on-orbit GOCE data with application over Indo-Pak region. *Tectonophysics*, *690*, 253–262.

Ferguson, J. F., Felch, R. N., Aiken, C. L. V., Oldow, J. S., & Dockery, H. (1988). Models of the Bouguer gravity and geologic structure at Yucca Flat, Nevada. *Geophysics*, *53*(2), 231–244.

Floberghagen, R., Fehringer, M., Lamarre, D., Muzi, D., Frommknecht, B., Steiger, C., et al. (2011). Mission design, operation and exploitation of the gravity field and steady-state ocean circulation explorer mission. *Journal of Geodesy*, *85*(11), 749–758. https://doi.org/10.1007/s00190-011-0498-3

Gladkikh, V., & Tenzer, R. (2012). A mathematical model of the global ocean saltwater density distribution. *Pure and Applied Geophysics*, *169*(1–2), 249–257.

Gómez-Ortiz, D., & Agarwal, B. N. P. (2005). 3DINVER. M: A MATLAB program to invert the gravity anomaly over a 3D horizontal density interface by Parker–Oldenburg's algorithm. *Computers & Geosciences*, *31*(4), 513–520.

Gómez-Ortiz, D., Agarwal, B. N. P., Tejero, R., & Ruiz, J. (2011). Crustal structure from gravity signatures in the Iberian Peninsula. *The Geological Society of America Bulletin*, *123*(7–8), 1247–1257. https://doi.org/10.1130/B30224.1

Grigoriadis, V. N., Tziavos, I. N., Tsokas, G. N., & Stampolidis, A. (2016). Gravity data inversion for Moho depth modeling in the Hellenic area. *Pure and Applied Geophysics*, *173*(4), 1223–1241.

Grombein, T., Seitz, K., & Heck, B. (2013). Optimized formulas for the gravitational field of a tesseroid. *Journal of Geodesy*, *87*, 645–660. https://doi.org/10.1007/s00190-013-0636-1

Heiskanen, W. A., & Moritz, H. (1967). *Physical geodesy*. New York: W. H. Freeman.

Hinze, W. J. (2003). Bouguer reduction density, why 2.67? *Geophysics*, *68*(5), 1559–1560. https://doi.org/10.1190/1.1620629

Hsieh, H.-H., Yen, H.-Y., & Shih, M.-H. (2010). Moho depth derived from gravity data in the Taiwan strait area. *Terrestrial, Atmospheric and Oceanic Sciences*, *21*, 235–241.

Jiang, W., Zhang, J., Tian, T., & Wang, X. (2012). Crustal structure of Chuan-Dian region derived from gravity data and its tectonic implications. *Physics of the Earth and Planetary Interiors*, *212–213*, 76–87.

Kiamehr, R., & Gómez-Ortiz, D. (2009, A new 3D Moho depth model for Iran based on the terrestrial gravity data and EGM2008 model. In *EGU General Assembly Conference Abstracts* (Vol. 11, p. 321).

Knapmeyer-Endrun, B., Krüger, F., & Group, t. P. W. (2014). Moho depth across the Trans-European Suture Zone from P- and S-receiver functions. *Geophysical Journal International*, *197*(2), 1048–1075.

Kvas, A., Mayer-Gürr, T., Krauss, S., Brockmann, J. M., Schubert, T., Schuh, W.-D., et al. (2019). *The satellite-only gravity field model GO-CO06s*. GFZ Data Services. https://doi.org/10.5880/ICGEM.2019.002

Laske, G., Masters, G., Ma, Z., & Pasyanos, M. (2013). Update on CRUST1. 0—A 1-degree global model of Earth's crust. *Geophysical Research Abstracts*, *15*, 2658.

Lebedev, S., Adam, J. M.-C., & Meier, T. (2013). Mapping the Moho with seismic surface waves: A review, resolution analysis, and recommended inversion strategies. *Tectonophysics*, *609*, 377–394.

Li, Y., Gao, M., & Wu, Q. (2014). Crustal thickness map of the Chinese mainland from teleseismic receiver functions. *Tectonophysics*, *611*, 51–60.

Meier, U., Curtis, A., & Trampert, J. (2007). Global crustal thickness from neural network inversion of surface wave data. *Geophysical Journal International*, *169*(2), 706–722.

Mooney, W. D., Laske, G., & Masters, T. G. (1998). CRUST 5.1: A global crustal model at 5° × 5°. *Journal of Geophysical Research*, *103*(B1), 727–747.

Moritz, H. (1990). The inverse Vening Meinesz problem in isostasy. *Geophysical Journal International*, *102*(3), 733–738.

Moritz, H. (2000). Geodetic reference system 1980. *Journal of Geodesy*, *54*(3), 395–405.

Nataf, H.-C., & Ricard, Y. (1996). 3SMAC: An a priori tomographic model of the upper mantle based on geophysical modeling. *Physics of the Earth and Planetary Interiors*, *95*(1), 101–122.

Novák, P., & Tenzer, R. (2013). Gravitational gradients at satellite altitudes in global geophysical studies. *Surveys in Geophysics*, *34*(5), 653–673.

Oldenburg, D. W. (1974). The inversion and interpretation of gravity anomalies. *Geophysics*, *39*(4), 526–536.

Parker, R. L. (1972). The rapid calculation of potential anomalies. *Geophysical Journal of the Royal Astronomical Society*, *31*, 447–455.

Phillips, D. L. (1962). A technique for the numerical solution of certain integral equations of the first kind. *Journal of the ACM*, *9*(1), 84–97.

Prasanna, H. M. I., Chen, W., & İz, H. B. (2013). High resolution local Moho determination using gravity inversion: A case study in Sri Lanka. *Journal of Asian Earth Sciences*, *74*, 62–70. https://doi.org/10.1016/j.jseaes.2013.06.005

Prutkin, I., & Saleh, A. (2009). Gravity and magnetic data inversion for 3D topography of the Moho discontinuity in the northern Red Sea area, Egypt. *Journal of Geodynamics*, *47*(5), 237–245.

Reamer, S. K., & Ferguson, J. F. (1989). Regularized two-dimensional Fourier gravity inversion method with application to the Silent Canyon caldera, Nevada. *Geophysics*, *54*(4), 486–496.

Reguzzoni, M., & Sampietro, D. (2015). GEMMA: An Earth crustal model based on GOCE satellite data. *International Journal of Applied Earth Observation and Geoinformation*, *35*, 31–43.

Reguzzoni, M., Sampietro, D., & Sansò, F. (2013). Global Moho from the combination of the CRUST2.0 model and GOCE data. *Geophysical Journal International*, *195*(1), 222–237.

Rui, F. (1985). Crustal thickness and densities in the upper mantle beneath China—The results of three dimensional gravity inversion. *Acta Seismologica Sinica*, *7*(2), 143–157.

Shapiro, N. M., & Ritzwoller, M. H. (2002). Monte-Carlo inversion for a global shear-velocity model of the crust and upper mantle. *Geophysical Journal International*, *151*(1), 88–105.

Shin, Y. H., Choi, K. S., & Xu, H. (2006). Three-dimensional forward and inverse models for gravity fields based on the Fast Fourier Transform. *Computers & Geosciences*, *32*(6), 727–738. https://doi.org/10.1016/j.cageo.2005.10.002

Shin, Y. H., Shum, C. K., Braitenberg, C., Lee, S. M., Na, S.-H., Choi, K. S., et al. (2015). Moho topography, ranges and folds of Tibet by analysis of global gravity models and GOCE data. *Scientific Reports*, *5*, 11681. https://doi.org/10.1038/srep11681

Shin, Y. H., Xu, H., Braitenberg, C., Fang, J., & Wang, Y. (2007). Moho undulations beneath Tibet from GRACE-integrated gravity data. *Geophysics Journal International*, *170*, 971–985. https://doi.org/10.1111/j.1365-246X.2007.03457.x

Sjöberg, L. E. (2009). Solving Vening Meinesz–Moritz inverse problem in isostasy. *Geophysical Journal International*, *179*(3), 1527–1536. https://doi.org/10.1111/j.1365-246X.2009.04397.x

Sjöberg, L. E., & Bagherbandi, M. (2011). A method of estimating the Moho density contrast with a tentative application of EGM08 and CRUST2.0. *Acta Geophysica*, *59*(3), 502–525. https://doi.org/10.2478/s11600-011-0004-6

Soller, D. R., Ray, R. D., & Brown, R. D. (1982). A new global crustal thickness map. *Tectonics*, *1*(2), 125–149.

Steffen, R., Steffen, H., & Jentzsch, G. (2011). A three-dimensional Moho depth model for the Tien Shan from EGM2008 gravity data. *Tectonics*, *30*, TC5019. https://doi.org/10.1029/2011TC002886

Tapley, B. D., Bettadpur, S., Ries, J., Thompson, P. F., & Watkins, M. M. (2004). GRACE measurements of mass variability in the Earth system. *Science*, *305*(5683), 503–505. https://doi.org/10.1126/science.1099192

Tapley, B. D., Bettadpur, S., Watkins, M., & Reigber, C. (2004). The gravity recovery and climate experiment: Mission overview and early results. *Geophysical Research Letters*, *31*, L09607. https://doi.org/10.1029/2004GL019920

Tenzer, R., & Chen, W. (2019). Mantle and sub-lithosphere mantle gravity maps from the LITHO1.0 global lithospheric model. *Earth-Science Reviews*, *194*, 38–56.

Tenzer, R., Chen, W., Tsoulis, D., Bagherbandi, M., Sjöberg, L. E., Novák, P., & Jin, S. (2015). Analysis of the refined CRUST1.0 crustal model and its gravity field. *Surveys in Geophysics*, *36*(1), 139–165.

Tenzer, R., Novák, P., & Gladkikh, V. (2011). On the accuracy of the bathymetry-generated gravitational field quantities for a depth-dependent seawater density distribution. *Studia Geophysica et Geodaetica*, *55*(4), 609–626. https://doi.org/10.1007/s11200-010-0074-y

Tenzer, R., Novák, P., Vajda, P., Gladkikh, V., & Hamayun. (2012). Spectral harmonic analysis and synthesis of Earth's crust gravity field. *Computational Geosciences*, *16*(1), 193–207. https://doi.org/10.1007/s10596-011-9264-0

Tenzer, R., Pavel, N., & Vladislav, G. (2012). The bathymetric stripping corrections to gravity field quantities for a depth-dependent model of seawater density. *Marine Geodesy*, *35*(2), 198–220. https://doi.org/10.1080/01490419.2012.670592

Tenzer, R., Vajda, P., & Hamayun, P. (2010). A mathematical model of the bathymetry-generated external gravitational field. *Contributions to Geophysics and Geodesy*, *40*(1), 31–44. https://doi.org/10.2478/v10126-010-0002-8

Tiberi, C., Diament, M., Lyon-Caen, H., & King, T. (2001). Moho topography beneath the Corinth Rift area (Greece) from inversion of gravity data. *Geophysical Journal International*, *145*(3), 797–808.

Tikhonov, A. (1963). Solution of incorrectly formulated problems and the regularization method. *Soviet Mathematics - Doklady*, *5*, 1035–1038.

Tikhonov, A. N., & Arsenin, V. Y. (1977). *Solutions of ill-posed problems*. Washington, DC: Winston and Sons.

Tirel, C., Gueydan, F., Tiberi, C., & Brun, J.-P. (2004). Aegean crustal thickness inferred from gravity inversion. Geodynamical implications. *Earth and Planetary Science Letters*, *228*(3), 267–280.

Turcotte, D. L., & Schubert, G. (2014). *Geodynamics*. Cambridge: Cambridge University Press.

Van der Meijde, M., Fadel, I., Ditmar, P., & Hamayun, M. (2015). Uncertainties in crustal thickness models for data sparse environments: A review for South America and Africa. *Journal of Geodynamics*, *84*, 1–18.

Van der Meijde, M., Julià, J., & Assumpção, M. (2013). Gravity derived Moho for South America. *Tectonophysics*, *609*, 456–467.

Vening Meinesz, F. A. (1931). Une Nouvelle Méthode Pour la Réduction Isostatique Régionale de L'intensité de la Pesanteur. *Bulletin Geodesique*, *29*, 33–51.

Wessel, P., Smith, W. H. F., Scharroo, R., Luis, J., & Wobbe, F. (2013). Generic mapping tools: Improved version released. *Eos Transactions American Geophysical Union*, *94*(45), 409–410.

Wild-Pfeiffer, F. (2008). A comparison of different mass elements for use in gravity gradiometry. *Journal of Geodesy*, *82*(10), 637–653. https://doi.org/10.1007/s00190-008-0219-8

Zhang, C., Huang, D., Wu, G., Ma, G., Yuan, Y., & Yu, P. (2015). Calculation of Moho depth by gravity anomalies in Qinghai–Tibet Plateau based on an improved iteration of Parker–Oldenburg inversion. *Pure and Applied Geophysics*, *172*(10), 2657–2668.